

# Investigation of combustion dynamics in a cavity-based combustor with high-speed laser diagnostics

Pradip Xavier<sup>1</sup> · Alexis Vandel<sup>1</sup> · Gilles Godard<sup>1</sup> · Bruno Renou<sup>1</sup> · Frédéric Grisch<sup>1</sup> · Gilles Cabot<sup>1</sup> · Mourad A. Boukhalfa<sup>1</sup> · Michel Cazalens<sup>2</sup>

Received: 15 September 2015 / Revised: 25 January 2016 / Accepted: 30 January 2016 / Published online: 16 March 2016  
© Springer-Verlag Berlin Heidelberg 2016

**Abstract** The dynamics of the flame/flow interaction produced in an optically accessible, premixed, and staged cavity-based combustor was investigated with high-speed particle image velocimetry (PIV) and OH-planar laser-induced fluorescence (OH-PLIF). The combined PIV and OH-PLIF images were recorded at 2.5 kHz to assess stabilization mechanisms occurring between the cavity and the mainstream. Dynamic pressure and global heat-release rate fluctuations were complementary measured. Important characteristics were identified for two operating conditions, differing from the ratio of momentum  $J$  (taken between the mainstream and the cavity jet): a high ratio of momentum ( $J = 7.1$ ) produced a “stable” flow, whereas a lower one ( $J = 2.8$ ) displayed “unstable” conditions. Analysis of the “unstable” case revealed an intense flow instability, primarily due to premixed flow rate fluctuations inside the cavity. This effect is confirmed from a proper orthogonal decomposition analysis of PIV data, which illustrates the prominent role of large-scale flow oscillations in the whole combustor. Furthermore, the simultaneous analysis of flow velocities and gas state (either unburned or burned) displayed important fluctuations inside the shear layer, reducing effective flame-holding capabilities. By contrast, the increase in the ratio of momentum in the “stable” case reduces significantly the penetration of the cavity flow into

the mainstream and consequently produces stable properties of the shear layer, being valuable to considerably improve flame stabilization.

## 1 Introduction

Growing environmental concerns has led to significant restrictions concerning pollutant emissions in gas turbines. Lean premixed combustion is a promising solution because it has the advantage of preventing high thermal loads at the turbine entry and being able to cutoff thermal  $\text{NO}_x$  emissions (Correa 1993; Wulff and Hourmouziadis 1997). However, the implementation of lean premixed combustion increases the risks of flashback, flame blow-off at partial load regimes, and possible combustion instabilities induced by thermoacoustic oscillations (Candel 2002). Integration of cavities in combustors could be used to improve flame stabilization, and extend lean blow-off limits of gas turbines (Lieuwen 2012). Among others, it is interesting to note the development of trapped vortex combustors (Hsu et al. 1998; Roquemore et al. 2001), rich-burn/quick-mix/lean-burn (RQL)-staged combustors (Straub et al. 2005), or even scramjet hypersonic applications (Ben-Yakar and Hanson 2001).

The effectiveness of these geometries lies on the presence of a shear layer at the flow separation, and important flow recirculation zones within the cavity (Pitz and Daily 1983; Ghoniem et al. 2005). Both contribute to improving the mixing between burned gases contained in the cavity and incoming lean mixtures. However, the flow dynamics of the separating shear layer in non-reacting conditions is subject to a variety of hydrodynamic instabilities (e.g., Kelvin–Helmholtz instability) (Ho and Huerre 1984; Dimotakis and Brown 1976), which can induce

✉ Pradip Xavier  
pxavier@imft.fr  
Michel Cazalens  
michel.cazalens@safran.fr

<sup>1</sup> CORIA UMR 6614, Normandie University, CNRS, University and INSA of Rouen, Av. de l'Université, Saint Etienne du Rouvray 76800, France

<sup>2</sup> Safran R&T, Paris, France

vortex shedding (Brown and Roshko 1974). In cavity flows, these instabilities can be amplified: The trailing corner of the opposite wall combined with the generation of vortical structures in the shear layer may induce large pressure and velocity fluctuations which can travel upstream. This might lead to undesired level of noises, and even self-sustained hydrodynamic oscillations (Rockwell and Knisely 1979; Cattafesta et al. 2008). Numerous studies have considered the primary mechanisms involved in the development of such instabilities in inert cavities (Rockwell and Knisely 1979; Little and Whipkey 1979). Gharib (1987) and Koenig and Roshko (1985) found that a “locked” vortex in the cavity led to an extremely stable flow topology, but very little fluid was exchanged between the cavity and the main channel. In addition to the natural flow entrainment (Sturgess and Hsu 1997), some authors suggested to directly inject mass into the cavity to improve mass transfers, and flame stabilization in combustion applications (Hsu et al. 1998). Unfortunately, these flows still remain unstable: The coupling between the complex flow dynamics and subsequent heat-release rate oscillations makes the design of such configurations more difficult due to the untold number of parameters (Altay et al. 2009). Therefore, an understanding of the stabilization mechanisms involved in a cavity-based combustor is of great importance. Moreover, experimental data could be used for numerical simulations, by providing suitable model validation.

As combustion dynamics must be both temporally and spatially resolved, high-speed laser imaging diagnostics are a well-adapted strategy to obtain measurements exhibiting instabilities. As mentioned by Bohm et al. (2011, 2013), the advent of Q-switched, all-solid-state, diode-pumped lasers and the emergence of complementary metal oxide semiconductor (CMOS) camera technologies made it possible to transfer planar optical diagnostic methods to the multi-kilohertz regime. Among the available high-speed optical diagnostics, high-speed OH-PLIF (Kaminski et al. 1999) and PIV (Upanietks et al. 2002) methods have proved to be suitable for combustion applications. Recent studies have implemented these laser diagnostics to investigate unsteady or transient mechanisms in academic turbulent flames and conventional gas turbine combustors for various scenarios: local extinction associated with vortex–flame interactions in opposed-jet flames (Bohm et al. 2009), estimation of flame dynamics, and consumption rates in a turbulent flame (Johchi et al. 2015), re-ignition in a jet diffusion flame (Steinberg et al. 2011), 3D-flame propagation in a turbulent flow (Trunk et al. 2013), flame blowout in swirl combustion (Stohr et al. 2011), PVC and flashback in LPP swirl flames (Boxx et al. 2010), flame kernel development in a GT, and ignition processes in internal combustion engines (Boxx et al. 2013; Peterson et al. 2014).

Even if many studies have considered reactive cavities operating with both supersonic and subsonic flows (Ben-Yakar and Hanson 2001; Yuan et al. 2015; Sun et al. 2015; Hsu et al. 1998; Roquemore et al. 2001), few studies have reported unstable operating conditions (Hsu et al. 1999; Roquemore et al. 2001), and no detailed investigations exist concerning mechanisms driving occurrence of these instabilities. Therefore, the objectives of the present study are to (1) implement simultaneous high-speed PIV and high-speed OH-PLIF in a complex geometry and to (2) investigate the combustion dynamics in an academic premixed cavity-based combustor displaying unstable and stable behaviors. The imaging system was applied on two operating conditions, differing from the ratio of momentum  $J$ , taken between the mainstream and the cavity jet: The first one exhibited self-sustained thermoacoustic oscillations, whereas the second one burned stably. The paper is organized as follows: the experimental setup, and test conditions are described in Sect. 2. Section 3 provides details concerning the laser measurement methods, and post-processing tools used to process the data measurements. An analysis is then carried out to examine the two operating conditions, and point out the mechanisms of flame stabilization in Sect. 4.

## 2 Burner and operating conditions

### 2.1 Burner design

Experiments were conducted in an existing test facility, which was previously used to study swirl injectors (Taupin et al. 2007; Burguburu et al. 2011). The main advantage of this setup is the presence of a fully annular transparent quartz tube, which can operate up to 0.5 MPa. Important modifications were performed and resulted in many constraints for the cavity-based combustor design. The burner is inserted into a Herasil cylindrical quartz tube with an inner diameter of 80 mm and a length of 200 mm. This quartz tube is surrounded by a second protective transparent casing equipped with planar quartz windows (not shown in Fig. 1). To avoid thermal and mechanical constraints, cooling air is injected in the gap between the casing and the cylindrical quartz tube. This cold air is also used to cool down exhaust gases (by means of dilution holes located downstream of the burner region). An adaptive nozzle, located at the burner outlet, is used to set the absolute pressure  $P_{ch}$  of the combustor to 0.17 MPa.

The cavity-based burner is shown in Fig. 1, and it consists of cylindrical forebody and afterbody elements, with a diameter of 59 mm and a corresponding main height of 10.5 mm. A smaller tube, with a length of  $L_c = 22$  mm, is used to assemble the two pieces and form an annular

**Fig. 1** Schematic illustration of the experimental setup

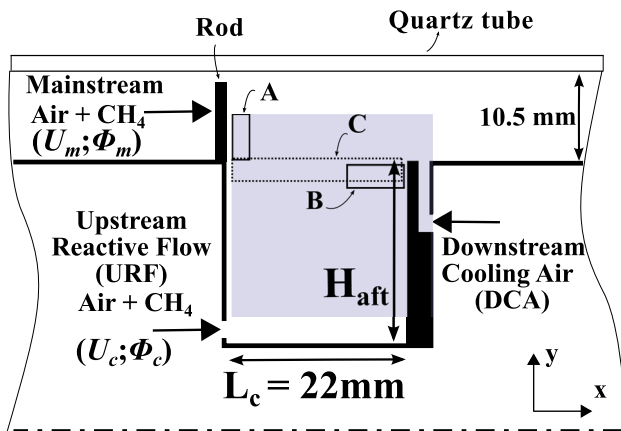
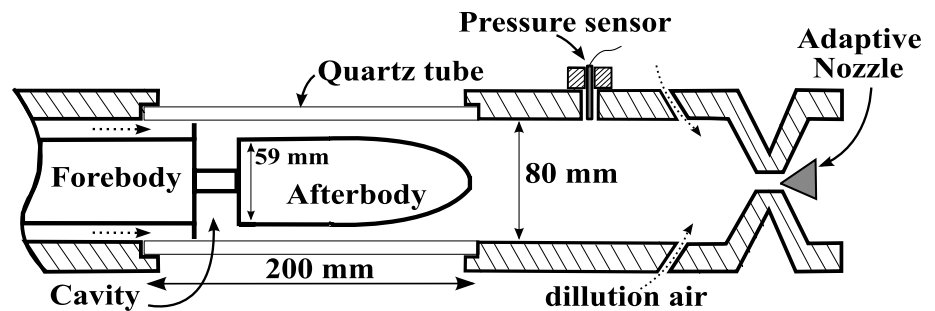


**Fig. 2** Details of the cavity-based combustor. Nomenclature and coordinates are presented. The grey square shows the region of interest for optical diagnostics

cavity located in the inner part of the quartz tube. With this configuration, boundary effects as well as asymmetries can be limited. Cavity dimensions are set according to results reported by Burguburu et al. (Burguburu et al. 2012) with an aspect ratio of  $L_c/H_{aft} = 1.19$ .

The cavity region is detailed in Fig. 2. The mainstream flow consists of a premixed mixture of air and methane ( $\text{CH}_4$ ) with a bulk velocity  $U_m$ , and an equivalence ratio  $\phi_m$ . It flows in the 10.5-mm high annular gap created between the forebody and the cylindrical quartz tube. To reduce acoustic coupling with the combustor system, the inlet is also choked using a sonic nozzle. Acting as secondary flame holders, 20 rods, each with a diameter of 3 mm, are positioned on the upstream cavity corner and produce a blockage area of 23 % in the mainstream.

The upstream reactive flow (URF) injection system delivers a premixed mixture of air and  $\text{CH}_4$  with a bulk velocity  $U_c$ , and an equivalence ratio  $\phi_c$ . This injection system is installed in the lower part of the upstream cavity face by means of a 1 mm annular slot. An additional injection system, named downstream cooling air (DCA), is used to cool down the cavity trailing edge, subject to large thermal constraints. Figure 2 displays cartesian coordinates, with  $x = 0$  located at the cavity leading edge and oriented in the

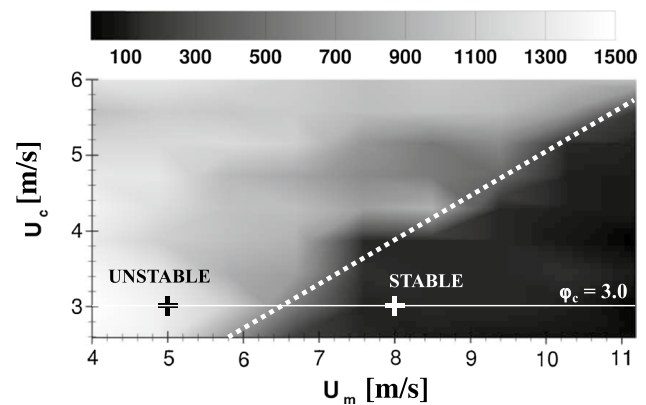


**Fig. 3** Stability map displaying the root mean square (RMS) of pressure fluctuations (in Pa) with varying  $U_m$  and  $U_c$ . Experiments conducted at a constant power  $P_g = 53.5$  kW. Crosses correspond to the operating conditions investigated in this study

direction of the mainstream. The  $y$ -axis is pointing in the mainstream. The corresponding velocity components in the coordinates  $(x, y)$  are  $(U_x, U_y)$ . The grey rectangle in Fig. 2 represents the field of interest for laser diagnostics. In addition, three zones of interest (A, B, C) are defined and will be used later for the data analysis (in Sect. 4): Zone A is located in the mainstream, zone B is in the downstream part of the cavity, next to the cavity trailing edge, and zone C includes the flow separation region between the main channel and the cavity (also named shear layer region).

## 2.2 Operating conditions

Experiments were conducted with a constant global power  $P_{glob}$  of 53.5 kW (constant power split between the mainstream and the cavity  $P_m/P_c$ ). Therefore, fuel mass flow rates were kept constant in this study. Preliminary results concerning the combustor stability are depicted in Fig. 3. It displays a stability map based on the root mean square (RMS) of pressure fluctuations in the combustor, with varying the bulk velocities  $U_m$  and  $U_c$  (by means of the air flow rate). As we were operating at a defined power, the equivalence ratios in the cavity and the mainstream flow were also modified.

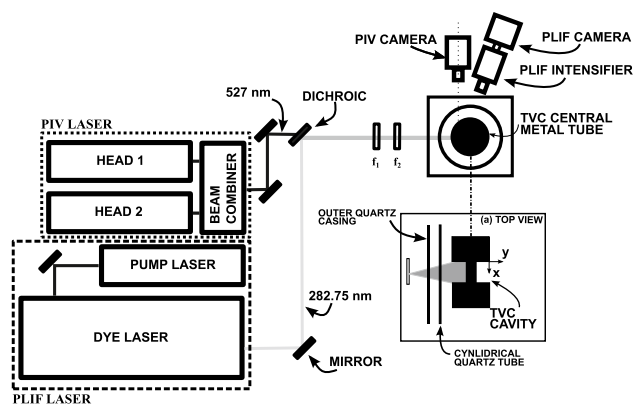
**Table 1** Operating conditions. The total power is conserved

		Unstable	Stable
Main	$U_m$ (m/s)	5.0	8.0
	$\phi_m$ (-)	0.8	0.7
	$P_m$ (kW)	50.0	50.0
Cavity	$U_c$ (m/s)	3.0	3.0
	$\phi_c$ (-)	3.0	3.0
	$P_c$ (kW)	3.5	3.5
Global	$P_{glob}$ (kW)	53.5	53.5
	$P_{ch}$ (MPa)	0.17	0.17
	$J$ (-)	2.8	7.1

It can be seen that the combustor exhibits either large or small pressure fluctuations. When  $U_c$  is relatively low and  $U_m$  relatively high, one can obtain a stable combustor. These findings are in agreement with the literature as this stable zone corresponds to large velocities in the mainstream (Roquemore et al. 2001; Hsu et al. 1998). In contrast, the combustor exhibits large pressure fluctuations when the mainstream air bulk velocity is decreased, or when the cavity air bulk velocity is increased. Based on preliminary measurements of Burguburu et al. (2012), who highlighted an optimum equivalence ratio in the cavity to obtain a stable configuration, the cavity equivalence ratio of the URF mixture was set to  $\phi_c = 3.0$ . This corresponds to a bulk velocity  $U_c = 3.0 \text{ m s}^{-1}$  (horizontal white line in Fig. 3). Two mainstream air flow rates were selected, representative of “stable” and “unstable” flows (crosses in Fig. 3). Similarly to Kumar and Mishra (2011b), the ratio of mainstream momentum to the cavity jet momentum  $J = \rho_m U_m^2 / \rho_c U_c^2$  ( $\rho$  being the density of the mixture at room temperature) is used to characterize each operating condition. The “unstable” case corresponded to a ratio of momentum  $J = 2.8$ , whereas in the “stable” case,  $J$  was increased to 7.1. Detailed operating conditions of each injection system are shown in Table 1.

### 3 Optical diagnostics and Image processing

Two high-speed laser-based measuring systems are used in this study: a OH-PLIF system, and a PIV system. Note that both systems are used at different repetition rates in order to obtain good signal-to-noise ratios. Only simultaneous data are analyzed. The region of interest is given in Fig. 2, and corresponds to a plane located in the spacing between two rods (see Sect. 2.1). Specific tools used to analyze measurements are described in this section.

**Fig. 4** Schematic representation of the dual measurement technique

#### 3.1 10-kHz OH-PLIF system

A high-speed OH-PLIF system operating at a repetition rate of 10 kHz was used to record the hydroxyl radical (OH) in the flame. A 10-kHz frequency-doubled, diode-pumped solid-state Nd:YAG laser (EdgeWave IS2011-E) operating at 532 nm (average power of 100 W) pumps a tunable dye laser (Sirah Credo) supplied with Rhodamine 590 dye. The resultant frequency-doubled output energy was 460  $\mu\text{J}/\text{pulse}$ . The energy in the probe volume was measured to 130  $\mu\text{J}/\text{pulse}$  (removing the optics used to create the laser sheet, and taking into account the two optical windows of the burner). The resultant laser beam was overlapped with the PIV beam by using a dichroic mirror and was expanded through a set of fused silica lenses (a spherical lens  $f_1 = 1000 \text{ mm}$  to create a focal spot, and a cylindrical diverging lens  $f_2 = -20 \text{ mm}$ ) to form a laser sheet of approximately 30 mm in height, and a thickness of 200  $\mu\text{m}$  (Fig. 4). Note that this resulted in a non-collimated sheet in the probe volume. The excitation wavelength was tuned to the  $Q_1(5)$  ro-vibronic transition of the  $A^2\Sigma^+(v' = 0) \leftarrow X^2\Pi(v'' = 1)$  band ( $\lambda = 282.75 \text{ nm}$ ). Daily adjustments to the excitation wavelength were performed using a laminar premixed  $\text{CH}_4/\text{air}$  flame. The detection system consists of an external image intensifier (HighSpeed IRO, LaVision) connected to a CMOS camera (Fastcam SA1) with a resolution of  $512 \times 512 \text{ pix}^2$  (21.5  $\text{pix}/\text{mm}$  magnification ratio). The UV lens (100 mm f/2 B-Halle Nachfl. GmbH) was mounted on a Scheimpflug system because the camera was tilted at a  $15^\circ$  angle (away from the laser sheet normal) due to the central metal body and the presence of the PIV camera. The intensifier gate was set to 500 ns, and background noise arising from elastic scattering of the particles used for PIV was reduced with a high-pass

colored optical filter (Schott WG305). A broadband collection strategy from 308 to 330 nm with a bandpass colored filter (Schott UG11) was chosen to improve the signal-to-noise ratio. The duration of the measurement was 2.18 s at 10 kHz, but the combined analysis with vector fields (see below) resulted in the extraction of only one out of every four PLIF images.

### 3.2 2.5-kHz PIV system

A high-speed PIV system operating at a repetition rate of 2.5 kHz is used in this study. Note that the repetition rate was chosen to obtain a sufficient spatial resolution for the camera. A double cavity Nd:YLF laser (Darwin-Duo, Quantronix) operating at 527 nm fired two laser beams, 15 and 30  $\mu\text{s}$  apart (depending on the operating conditions). The laser beams were transmitted and combined with the UV laser beam through the dichroic mirror and expanded through the same lenses used for the PLIF beam. The laser thickness of the PIV beam was 500  $\mu\text{m}$ . 1  $\mu\text{m}$  zirconium dioxide  $\text{ZrO}_2$  particles were seeded through the various flow injection systems (by means of fluidized beds). The estimated Stokes number was 0.06 (based on the cavity length and the mainstream bulk velocity), being sufficient enough to track the flow. Moreover, the laser thickness was sufficiently thin in comparison to the vector spacing, so that calculation of derived 2D-quantities was precise enough. Mie scattering was collected on a 5-kHz high-speed CMOS camera (Phantom V10) equipped with a Nikon f/2.8 105 mm lens. The camera was set to a resolution of  $480 \times 480 \text{ pix}^2$ , resulting in a 24 pixel/mm magnification ratio. Distortion created by the cylindrical window were limited (less than 2 pixels) but systematically corrected with the use of a calibration target. However, due to important reflections, the field of view was reduced, and it was not possible to capture the entire mainstream flow passage (see Fig. 2). PIV Images were dewarped, and processed with a multi-pass interrogation window algorithm (DynamicStudio, Dantec) resulting in a final interrogation window of  $32 \times 32 \text{ pix}^2$  and a 50 % overlap. A median filter (effective only if the peak ratio was lower than 1.3) was applied as a vector post-processing routine. At 2.5 kHz, the system operated over 6.0 s durations with a vector spacing of 0.7 mm. The vector resolution was estimated with the method of Foucaut et al. (2004). This method is based on the PIV transfer function, which can be modelled as a cardinal sine (low-pass system). The cutoff frequency is chosen when the gain of this function is reduced by 3 dB. In the present conditions, it resulted in a range of resolved scales lying between 2.5 and 18 mm. Note that in our study, the investigation of relatively large scales was of interest, in order to improve the understanding of stabilization mechanisms in both conditions.

### 3.3 Additional measurement techniques

In order to further understand thermoacoustic oscillations, a dynamic pressure sensor (Kistler 7061B ThermoComp, 10 kHz sampling rate) was mounted on a waveguide system, 280 mm downstream from the cavity region (Fig. 2). Due to the spatial offset between the reaction zone the location of the pressure sensor, a temporal correction was performed, assuming a mean temperature of 1700 K, obtained by Merlin (2012). A sensitivity analysis showed that an uncertainty of  $\pm 400 \text{ K}$  on the temperature of burned gases led to a phase shift of less than  $1^\circ$  (taking the fundamental acoustic period as a reference). Acoustic mode detection was performed with one-sided power spectral densities (PSD) and the Welch method (Welch 1967). Results are given as sound pressure levels (SPL, units in  $\text{dB Hz}^{-1}$ ) with a frequency resolution of  $\pm 5 \text{ Hz}$ . Temporal fluctuations in the global heat-release rate were collected on a 10 kHz sampling rate photo multiplier tube (PMT, Hamamatsu 6780-20) with a selected photocathode of 0.15-nA low dark current. The output signal of the PMT was amplified with a Hamamatsu C7319 pre-amplifier ( $10^6$  gain). A BG12 band-pass optical filter was used to record spontaneous  $\text{CH}^*$  emission, thus providing a signal characteristic to follow heat-release rate fluctuations (Najm et al. 1998).

### 3.4 Image Processing

#### 3.4.1 Combustion dynamics

As the burner is staged and involves a large recirculation region, attempt to extract the location of the reaction zone or OH molar fraction with OH-PLIF images is not suitable due to the long lifetime of this radical in burned gases. However, access to the location of burned gases provides information on the effectiveness of the flame stabilization in the vicinity of the shear layer. An image processing tool was then developed to estimate locally the gas state, being either unburned or burned. With OH-PLIF images, the dimensionless variable  $p$  is defined as

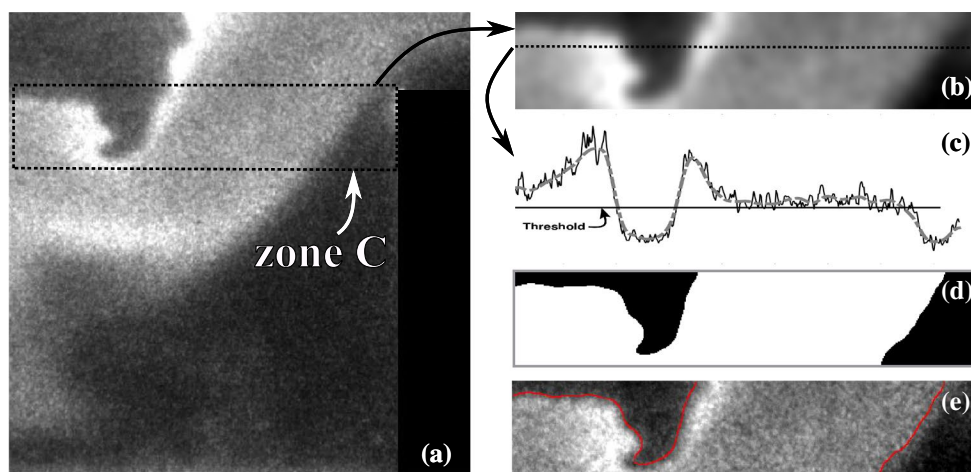
$$p = \mathfrak{B}(I_{\text{OH}}). \quad (1)$$

In Eq. 1,  $I_{\text{OH}}$  corresponds to the pixel intensity of OH-PLIF signals, and  $\mathfrak{B}(-)$  is a binarization operator. Note that the variable  $p$  is quite similar to the classical progress variable (Peters 2000). Therefore,  $p$  can take two values:  $p = 0$  corresponds to unburned gases, whereas  $p = 1$  corresponds to burned gases.

Figure 5 presents the method used to calculate  $p$ . First, OH-PLIF images were corrected to take into account the spatial inhomogeneity of the laser sheet profile with acetone-PLIF images recorded in the chamber filled with a homogeneous mixture of acetone vapor and air. The limited



**Fig. 5** Post-processing steps to determine the gas state dimensionless variable  $p$  from OH-PLIF images



optical distortion caused by the oblique viewing angle and the curved face of the quartz tube was systematically corrected with a calibrated target. A typical OH-PLIF image is shown in Fig. 5a. Pixel-to-pixel noise contained in the images was suppressed using a nonlinear diffusive filter (NLDF) adopting the following diffusive scheme (Weickert 1997):

$$\partial_t I = \nabla \cdot (D \nabla I), \quad (2)$$

where  $I$  and  $D$  are the intensity of a pixel and the local diffusivity, respectively. The definition of  $D$  was chosen according to Charbonnier et al. (1994) and was updated at each time step (i.e., nonlinear diffusion). A filtered image is depicted in Fig. 5b. Two extracted profiles in Fig. 5c show more precisely the diffusive effect of the filter on the fluorescence levels (black line: raw profile, gray line: filtered profile). Finally, an automatic binarization algorithm (Otsu 1979) was applied on the filtered images to segregate burned and unburned gases (for instance the threshold in Fig. 5c, d). Figure 5e compares a raw image with the binarized one (red line). With this procedure, the choice of the threshold could affect the accuracy of the parameter  $p$ . A sensitivity study, by artificially changing by  $\pm 10\%$  the threshold value obtained with the present method resulted in a variation of  $\pm 5\%$  on the final values of  $p$ . In view of the results given in Sect. 4, this uncertainty is negligible on the analysis performed in this study.

### 3.4.2 Proper orthogonal decomposition (POD)

A particular attention must be paid to effects of the periodic instability on the flow field: existence of coherent flow motions and energy associated with these coherent motions. Phase-averaging is a common tool which could be implemented with the periodic pressure trace. With this method, it is possible to obtain the mean velocity evolution along one instability cycle. However, in some cases, the phase

averaged mean flow could be difficult to estimate, and may lead to a biased estimation of the turbulent kinetic energy. Similarly, a Fourier transform analysis only provides the energy contribution of a specific frequency. Therefore the choice of the cutoff frequency can affect results. Therefore, to report the energy associated with the whole periodic instability and to be non-dependant on the cutoff frequency, the POD appears to be an interesting tool. Theory of the POD is well established, and the reader can refer to studies which give a detailed description of this approach (Berkooz et al. 1993; Cordier and Bergmann 2002). In the present study, the POD is applied to velocity components to highlight the presence of periodic flow motions responsible for flow instability. The POD technique consists in the decomposition of the velocity field  $u(\mathbf{x}, t)$  as

$$u(\mathbf{x}, t) \approx \sum_{k=1}^K a_k(t) \Phi_k(\mathbf{x}), \quad (3)$$

where  $\mathbf{x}$  is a vector containing the velocity components,  $\Phi_k(\mathbf{x})$  are space functions,  $a_k(t)$  are temporal coefficients, and  $K$  is a positive integer used to approximate the variable of interest  $u(\mathbf{x}, t)$ . Space functions  $\Phi_k$  are usually defined *a priori* (e.g., sin or cos functions in the case of a Fourier transform). In contrast, the POD directly uses the original data  $u(\mathbf{x})$  and an energetic criterion to estimate these functions. Mathematically, it corresponds to maximize the projection of the variable of interest  $u$  on the space function  $\Phi$  and corresponds to an eigenvalue problem (i.e.,  $Ax = \lambda x$ ).  $\lambda$  are the eigenvalues associated with the eigenfunctions  $\Phi$ . Therefore, individual eigenvalue  $\lambda_k$  represents the contribution of the  $k$ th mode to the overall turbulent kinetic energy (taking velocity fluctuations into account). The advantage of POD is that it produces a set of eigenmodes, which represent spatial coherences within the flow. Moreover, these eigenmodes are ordered according to the turbulent kinetic energy. Note that the direct method (i.e., spatial correlation

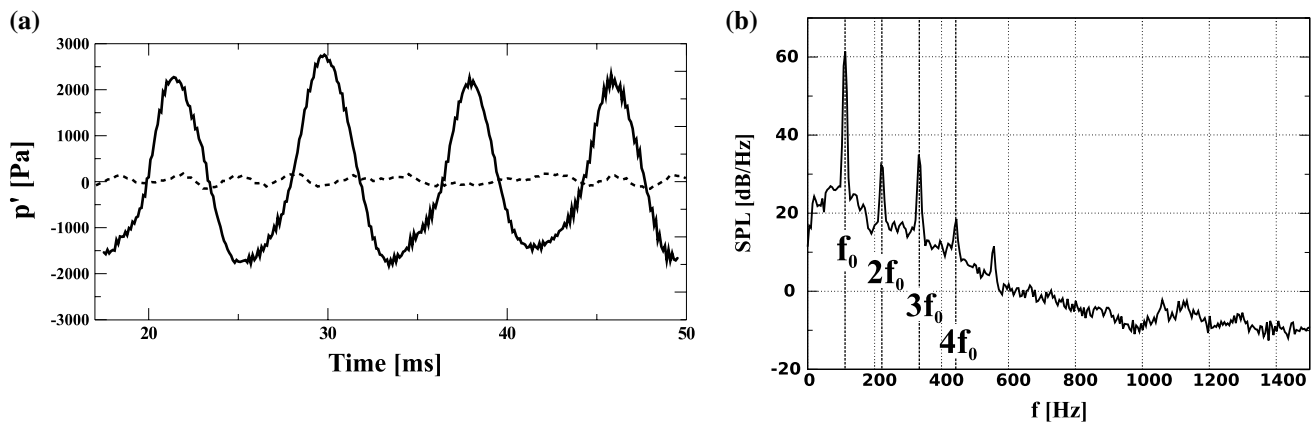


**Fig. 6** **a** Time evolution of pressure fluctuations for the “unstable” (*line*) and “stable” (*dashed line*) operating conditions (see Table 1). **b** Pressure spectrum of the “unstable” case

matrix) was implemented as the number of grid points in each velocity field was much lower than the total number of PIV snapshots.

## 4 Results and discussion

This section aims to highlight the key flame stabilization mechanisms occurring in the cavity-based combustor. First, a description of the flow/flame dynamics encountered in the two operating conditions is presented. Then, the effect of the oscillatory flow motion as well as shear layer properties on flame stability are discussed in details.

### 4.1 Phenomenological description of the unstable and stable cases

Figure 6a depicts time series of pressure recorded for both operating conditions given in Table 1. The unstable case exhibits large and cyclic pressure fluctuations, measured at  $p'_{\text{rms}} = 1430$  Pa. In contrast, low-pressure fluctuation levels are observed in the stable case, with no more cyclic behavior. The corresponding pressure spectrum of the unstable case is presented in Fig. 6b and displays large peaks at a fundamental frequency of  $f_0 = 122$  Hz, and the others at its harmonics. Note that the pressure spectrum of the stable case exhibits a broadband spectrum, with no narrow peaks.

In order to study the flame/turbulence interactions between the flow and gas state (i.e., unburned or burned) in the combustor, typical series of measurements are presented in Figs. 7 and 8 for the unstable and stable case, respectively. Figure 7 depicts a typical sequence of instantaneous measurements representing the coupling of the velocity vector fields colored by their corresponding magnitudes and locations of burned gases (OH fluorescence levels in grayscale). The corresponding pressure and

heat-release rate values are also given in the graph at the bottom, on the right in Fig. 7 (numbered red dots).

Instantaneous analysis of the combustion instability cycle in the unstable case reveals that the zone close to the URF jet injection system is highly unstable: instead of flowing constantly, intense puffs can be observed, contributing to the flow unsteadiness into the cavity. Indeed, several vortices are established in Fig. 7#7, whereas almost null velocities are found in Fig. 7#3. In turn, the premixed flow rate injected into the combustor is changed and may explain the large heat-release rate oscillations. A direct consequence of these flow rate oscillations is visible in the downstream part of the cavity. A high radial velocity region, referred to “jet ejection process,” intermittently disturbs the shear layer established at the flow separation (dashed white circle in Fig. 7#1). These important fluctuations in the cavity also impacts the mainstream flow. Figure 7 highlights a significant flow unsteadiness in the main channel. Instead of flowing continuously above the cavity, lean flow puffs are visible (Fig. 7#4 and #2). Note that these puffs are correlated with the cavity flow topology: when the “jet ejection process” is preponderant, it completely penetrates into the mainstream channel, and null velocities in the vicinity of the shear layer are observed. In contrast, when cavity velocities are almost null, mainstream velocities next to the cavity opening are quite large. Another consequence of this flow instability is the location of burned gases (via the OH traces), which exhibits large fluctuations, being either in the mainstream (Fig. 7#1 and #7) or in the shear layer (Fig. 7#5). Note that analysis of high-speed images do not reveal any periodic disturbances due to the cylindrical flame holders located in the mainstream flow passage, confirming previous measurements (Burguburu et al. 2012).

Analysis of this sequence infers that the cavity flow unsteadiness is piloted by fluctuations of the URF flow rate, and finally greatly modifies the flow topology (“jet ejection

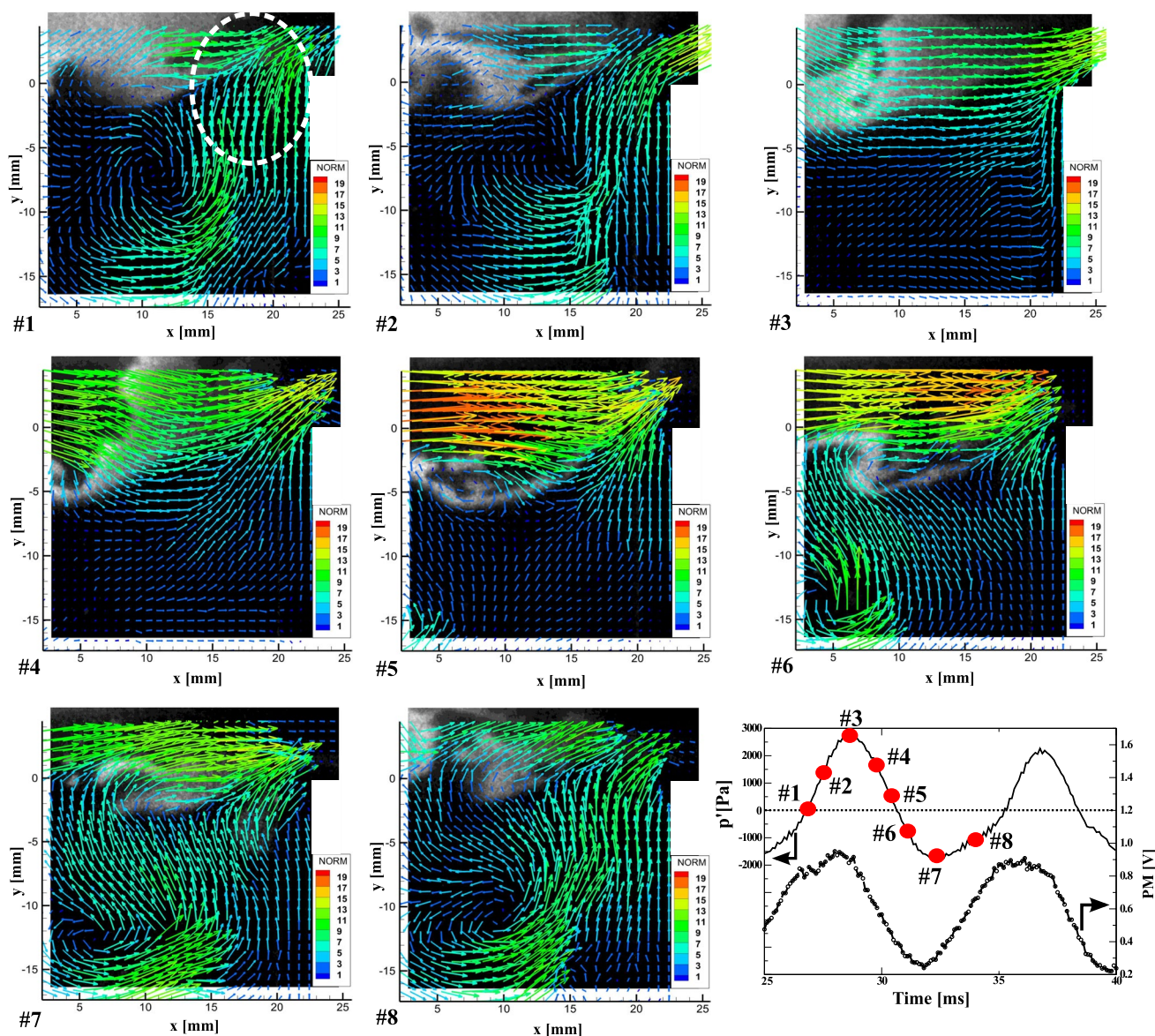


**Fig. 7** Simultaneous OH Traces and velocity measurements (colored according to magnitude) for an individual pressure cycle in the unstable case

process”), the heat-release rate, and the dynamic pressure. Analysis of high-speed measurements in the shear layer region also shows the absence of vortex shedding in the present configuration, contrary to results observed in backward-facing step or dump combustors (Altay et al. 2009). It is worth noting that the URF mass injection inside the cavity completely changes the flow topology, and may annihilate the vortex shedding process occurring in conventional shear layers. Experimental results confirm that the intense flow dynamics into the cavity alternately creates relatively large vortices, and therefore produces a modification of chemical reactions (e.g., local equivalence ratio) and hence heat-release rate. These strong oscillations interfere with

the shear layer, which is completely destabilized, and not favorable to produce robust flame-holding capabilities for the main lean mixture.

Figure 8 presents various snapshots for the “stable” case. It depicts the absolute velocity field, colored by the magnitude. In contrast with the “unstable” case, the snapshots present strong similarities. The velocity field in the cavity is quite homogeneous, with the presence of two counter-rotative vortices (see white streamlines in Fig. 8# 4). Burned gases are located in two specific regions. First, a long and thin ligament of OH traces is located all along the flow separation at  $y = 0$  mm. Second, a zone in the mainstream, is established for  $y > 3$  mm, with an axial location



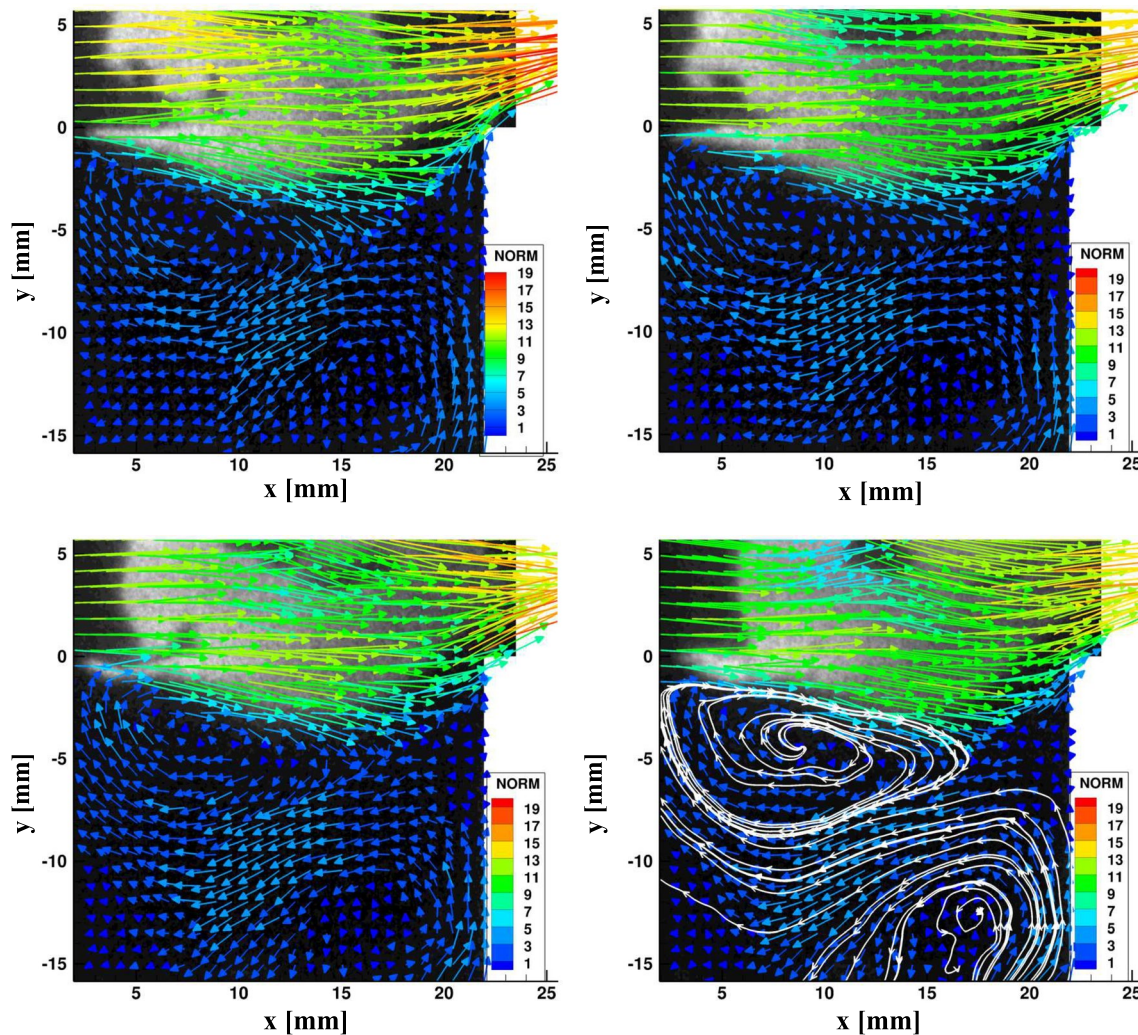


**Fig. 8** Simultaneous OH Traces and velocity measurements (colored according to magnitude) for the stable case. Time between each snapshot is 800  $\mu$ s. In #4, white lines correspond to streamlines

at  $x = 5$  mm. A zone of unburned gases intermittently appears between the two regions ( $0 \text{ mm} < y < 3 \text{ mm}$  and  $x < 7 \text{ mm}$ ), primarily due to the flow separation. Indeed, the URF mixture entering the cavity is rich (i.e.,  $\phi_c = 3.0$ ), and cannot burn as it is above the flammability limit. This statement is confirmed when inspecting images in Fig. 7: no OH traces are found in the cavity. Therefore, this rich mixture must mix with the incoming lean mainstream, established between the cavity opening and the lean mainstream flow. The incoming mainstream flow mixes with the cavity rich mixture in the vicinity of the shear layer, and lowers the local equivalence ratio. Then, radicals arising from the rich combustion enable ignition of the main mixture, slightly downstream of the cavity leading edge. This stable case clearly demonstrates that the main lean flame is stabilized by the use of the rich mixture injected

in the cavity, and mixing occurring in the shear layer. Note that this statement is in agreement with data from Fig. 3: when the cavity equivalence ratio is reduced, by keeping a  $J$  value relatively high, the burner is found to be unstable. Moreover, the ratio of mainstream momentum to the cavity jet momentum  $J$ , is more important in the stable case. This contributes to confine more the cavity flow dynamics (by reducing the effect of the “jet ejection process”), and thus, force the combustion dynamics to occur within the shear layer. This is also in agreement with the stability map in Fig. 3, and with previous works (Kumar and Mishra 2011a, b), which demonstrated the importance of this parameter to control the overall flow. Therefore, this aerodynamic parameter, combined with the cavity equivalence ratio could be used to obtain valuable characteristics in the shear layer for flame stabilization.

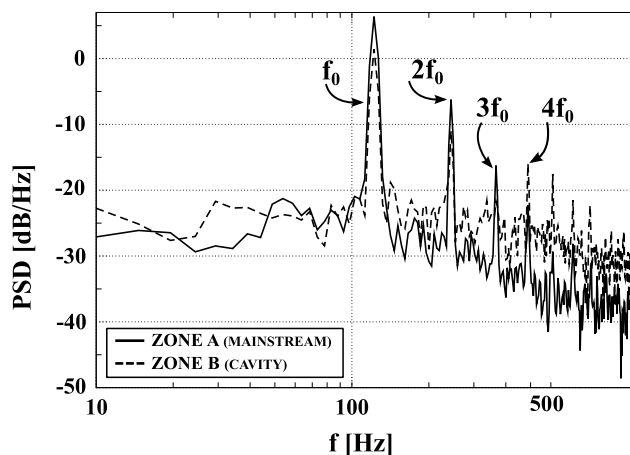


**Fig. 9** Power spectrum density of the axial velocity fluctuation  $u'_x$  in zone A (mainstream), and radial velocity fluctuation  $u'_y$  zone B (cavity). Refer to Fig. 2 for the nomenclature

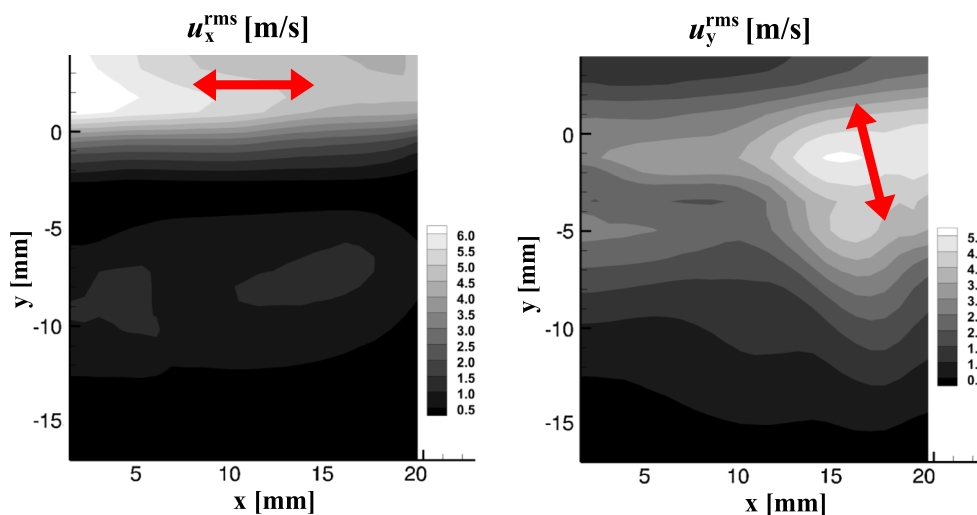
## 4.2 Unsteady flow characterization

This section focuses on obtaining an improved understanding of the flow dynamics, responsible for the large pressure and heat-release rate fluctuations. Regarding the “unstable” case, Figure 9 presents the PSD of the axial velocity fluctuation  $u'_x$  and radial velocity fluctuation  $u'_y$  in zones A and B, respectively (see Fig. 2). Results clearly show that the frequency of peaks are in accordance with the ones observed on the pressure spectrum. In addition, as these peaks are retrieved regardless of the zone investigated, it confirms that the fluid-coherent features do not originate from a local vortex shedding mechanism. Thus, thermoacoustic oscillations induce large-scale and periodic flow

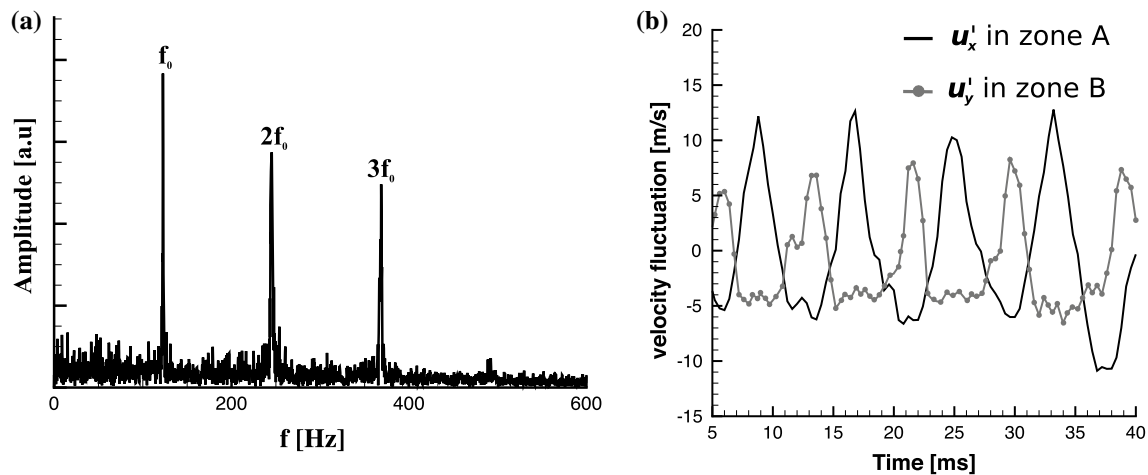
fluctuations in the whole combustor. However, the different peaks observed in Fig. 9 could be associated with different flow motions. Therefore, the use of the POD is adapted to spatially highlight these flow motions.

In order to evaluate the most energetic periodic flow motions and reconstruct a low-dimensional description of the flow field, a spatiotemporal proper orthogonal decomposition (POD) was performed. The method was applied to the velocity fluctuation fields. Eigenvalues show that the first POD mode contains approximately 70 % of the total turbulent kinetic energy. In contrast with many inert turbulent flows, the energy produced by the thermoacoustic oscillations is considerably huge. Therefore, a low-order reconstruction of the instantaneous velocity vector fields was performed by considering only the first POD mode. The RMS of each velocity component was estimated and results are shown in Fig. 10. The resultant fields reveal axial fluctuations in the main channel, whereas the “jet ejection process” is also visible when analyzing radial fluctuations. As explained in Sect. 4.1, the URF flow oscillations produce large flow fluctuations (“jet ejection process”), and destabilize the shear layer.

These results show that instabilities are fed by two energetic zones. In order to further elucidate the coupling between these zones, the axial and radial velocities extracted from the low-dimensional flow field are plotted in Fig. 11. First, the spectrum of the temporal coefficient of the first mode proves that the most energetic flow features periodically oscillate at the same acoustic frequency  $f_0$ . Note that the spectrum also includes subsequent peaks, which proves that the spatial mode depicted in Fig. 10 is the only large periodic flow motion involved in the unstable operating condition. Second, time history of velocity

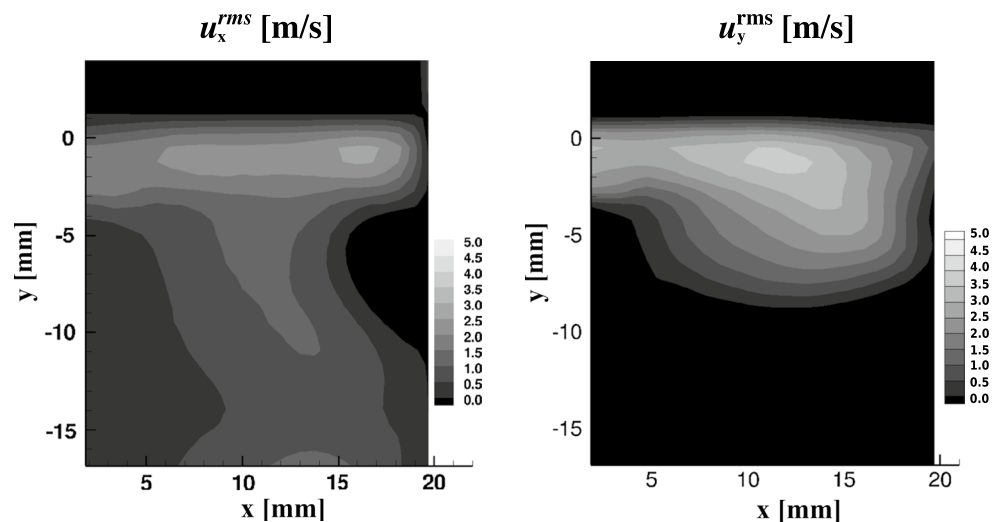


**Fig. 10** RMS of the velocity fields of the unstable case, reconstructed with the first POD mode. Left  $u_x^{\text{rms}}$ . Right  $u_y^{\text{rms}}$



**Fig. 11** **a** Power spectra of first POD coefficient. **b** Time history of velocity fluctuations in zone A and B, reconstructed with the first POD eigenmode

**Fig. 12** RMS of the velocity fields of the stable case. *Left*  $u_x^{rms}$ . *Right*  $u_y^{rms}$



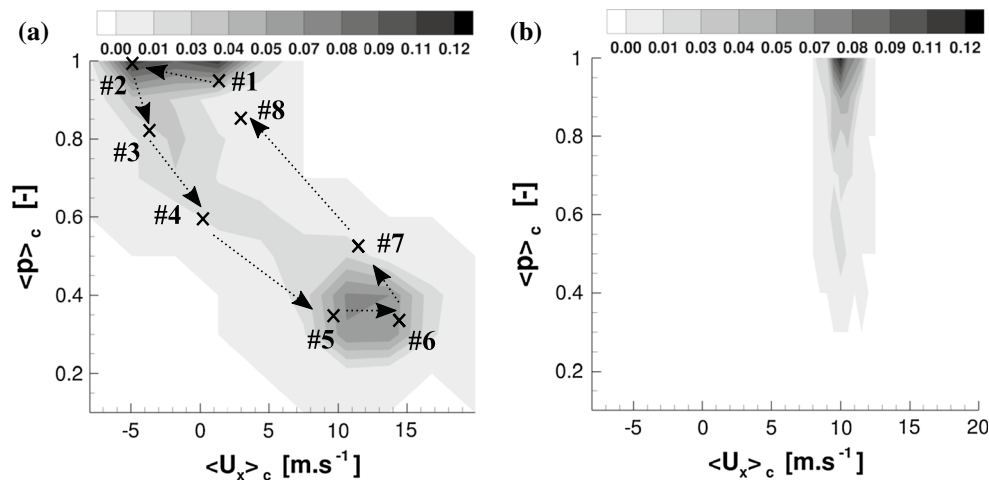
fluctuations (extracted from POD) within zone A and C are out of phase, thus reinforcing the hypothesis that the shear layer is fully modified by these large alternation of velocity fluctuations between the cavity and the main flows.

Figure 12 presents the RMS of axial velocities, which have been calculated with PIV raw data (no more periodic motion in this condition). Main part of flow fluctuations is located in the vicinity of the shear layer ( $y = 0$  mm). As the ratio of momentum  $J$  is larger in the stable case, velocity gradients are increased, thus creating more fluctuations. Moreover, the cavity is aerodynamically more confined, and interactions between the mainstream and the cavity are solely localized into the shear layer. Therefore, increasing the mainstream momentum changes the global flow topology, restrain flow fluctuations to the flow separation, and eventually contributes to the main flame stability.

### 4.3 Combustion dynamics

As mentioned in the previous section, the increase in the ratio of momentum  $J$  was found to aerodynamically confine the cavity and create a stable shear layer. In order to confirm the role of the shear layer on the flame stability, a simultaneous analysis of the flow and OH-fields in zone C was performed. Instantaneous axial velocity as well as the instantaneous gas state was extracted in the zone C, presented in Fig. 2. The latter was estimated by calculating the spatial averaged dimensionless variable  $\langle p \rangle_c$  (See Sect. 3.4.1). Results are depicted in Fig. 13, and display two joint probability density functions (pdfs), which were calculated with a sample of 5000 data. It shows the probability to encounter a pair of  $(\langle p \rangle_c, \langle U_x \rangle_c)$  values.

Figure 13a presents the joint pdf of the “unstable” case. A bimodal distribution, segregating between  $\langle p \rangle_c = 1$  and



**Fig. 13** Joint probability density functions (pdfs) in zone C of the spatially averaged dimensionless variable  $\langle p \rangle_c$  with the corresponding averaged axial velocity i.e.,  $\langle U_x \rangle_c$ . 5000 instantaneous data were considered. **a** pdf of the unstable case. **b** pdf of the stable case

$\langle p \rangle_c = 0.35$  is observed. When the shear layer contains majority of burned gases ( $\langle p \rangle_c = 1$ ), the axial velocities are quite low, revealing that the mainstream flow is ignited but is at the same time disturbed by the “jet ejection process”. Note that the appearance of negative velocities increases risks of flash-black in the main channel. In contrast, when axial velocities are large, the shear layer contains less burned gases, and demonstrates that the dynamic momentum of the mainstream flow completely drains burned gases from this region. To confirm these findings, several instantaneous data were added on the pdfs (Fig. 13a). These data correspond to black crosses and numbering is identical to Fig. 7. It is clearly visible that the shear layer properties are oscillating between the two peaks of the pdf, and with a defined path. Thus, great differences in both velocities and gas state contribute to the shear layer unsteadiness.

The joint pdf of the stable case (Fig. 13b) presents a different feature. Indeed, the pdf has a single peak, located at  $\langle p \rangle_c = 1$ , and  $\langle U_x \rangle_c = 10 \text{ m s}^{-1}$ . Increase in the mainstream momentum radically modifies the characteristics of the shear layer, composed in major part of burned gases, and with low velocity fluctuations. Then, the stability of the shear layer clearly contributes to a better flame stabilization.

## 5 Conclusion

A premixed and staged, cavity-based combustor was experimentally investigated by analyzing high-speed laser diagnostics data. Particle image velocimetry (PIV) and planar laser-induced fluorescence on the OH radical (OH-PLIF) were simultaneously implemented to study the flow and combustion dynamics. A binarization image processing

routine as well as a proper orthogonal decomposition tool were used to detect burned gases and most dominant energetic fluid structures, respectively. Two operating conditions were investigated: The first one exhibited strong oscillations, whereas the second one burned stably. These two conditions only differed in the mainstream momentum, which was larger in the stable case.

Analysis of the “unstable” case revealed intense pressure fluctuations (at 122 Hz), originating from premixed flow rate oscillations of the cavity jet injection. As a result, the combustion and flow dynamics are greatly affected and modify strongly the stability of the shear layer between the cavity and the main channel (via the “jet ejection process”). A proper orthogonal decomposition (POD) confirmed large flow fluctuations in the whole combustor, creating a “pulse”-like combustion dynamics (pulsing at the same acoustic frequency). It should be noted that in our operating conditions, the classical vortex shedding is not the most dominant mechanism driving the self-sustainment of the present instability. The “stable” case burned stably, with no distinct instability (broadband pressure spectrum). Moreover, the shear layer region is quite stable and primarily contributes to the efficient flame stabilization.

This study put in evidence the importance of the shear layer stability, producing effective flame-holding capabilities. Indeed, burned gases and moderate velocity fluctuations in this region enable to take advantage of the inherent fast mixing between the rich and lean stages of the combustor. Even if this study was focused on particular injection systems, large value of the ratio of momentum between the cavity and mainstream flows  $J = \rho_m U_m^2 / \rho_c U_c^2$  is found to be valuable to control the cavity confinement and yield a better mixing in the shear layer region. This also demonstrates that the range of operating conditions could be



extended as far as the cavity flow/combustion dynamics is sufficiently confined by the mainstream flow. Ongoing works are performed to further understand the acoustic coupling and occurrence of thermoacoustic oscillations.

**Acknowledgments** The research leading to these results has received funding from the European Community's Seventh Framework Programme (FP7/2007-2013) under Grant Agreement No. ACP0-GA-2011-265586.

## References

- Altay H, Speth R, Hudgins D, Ghoniem AF (2009) Flame-vortex interaction driven combustion dynamics in a backward-facing step combustor. *Combust Flame* 156:1111–1125
- Ben-Yakar A, Hanson R (2001) Cavity flame-holders for ignition and flame stabilization in scramjets: an overview. *J Propuls Power* 17(4):869–877
- Berkooz G, Holmes P, Lumley J (1993) The proper orthogonal decomposition in the analysis of turbulent flows. *Ann Rev Fluid Mech* 25:539–575
- Bohm B, Geyer D, Gregor M, Heeger C, Nauert A, Schneider C, Dreizler A (2013) Advanced laser diagnostics for understanding turbulent combustion and model validation. In: *Flow and combustion in advanced gas turbine combustors*, vol 1581. Springer, pp 93–160
- Bohm B, Heeger C, Boxx I, Meier W, Dreizler A (2009) Time-resolved conditional flow field statistics in extinguishing turbulent opposed jet flames using simultaneous highspeed PIV/OH-PLIF. *Proc Combust Inst* 32(2):1647–1654
- Bohm B, Heeger C, Gordon R, Dreizler A (2011) New perspectives on turbulent combustion: multi-parameter high-speed planar laser diagnostics. *Flow Turbul Combust* 86:313–341
- Boxx I, Carter C, Stohr M, Meier W (2013) Study of the mechanisms for flame stabilization in gas turbine model combustors using kHz laser diagnostics. *Exp Fluids* 54(5):1–17
- Boxx I, Stohr M, Carter C, Meier W (2010) Temporally resolved planar measurements of transient phenomena in a partially premixed swirl flame in a gas turbine model combustor. *Combust Flame* 157(8):1510–1525
- Brown G, Roshko A (1974) On the density effects and large structure in turbulent mixing layers. *J Fluid Mech* 64(04):775–816
- Burguburu J, Cabot G, Renou B, Boukhalfa A, Cazalens M (2011) Effects of  $\text{H}_2$  enrichment in flame stability and pollutant emissions for a kerosene/air swirled flame with an aeronautical fuel injector. *Proc Combust Inst* 33:2927–2935
- Burguburu J, Cabot G, Renou B, Boukhalfa A, Cazalens M (2012) Flame stabilization by hot products gases recirculation in a Trapped Vortex Combustor. In: *Proceedings of the ASME, Copenhagen, Denmark*, pp GT2012-68451
- Candel S (2002) Combustion dynamics and control: progress and challenges. *Proc Combust Inst* 29(1):1–28
- Cattafesta LN, Song Q, Williams DR, Rowley C, Alvi F (2008) Active control of flow-induced cavity oscillations. *Prog Aerosp Sci* 44:479–502
- Cordier L, Bergmann M (2002) Proper orthogonal decomposition: an overview. In: *Lecture series 2002–2004 on post-processing of experimental and numerical data*. Von Karman Institute for Fluid dynamics
- Correa S (1993) A review of  $\text{NO}_x$  formation under gas-turbine combustion conditions. *Combust Sci Technol* 87(1–6):329–362
- Dimotakis P, Brown GL (1976) The mixing layer at high Reynolds number: large-structure dynamics and entrainment. *J Fluid Mech* 78(3):535–560
- Foucaut J, Carlier J, Stanislas M (2004) PIV optimization for the study of turbulent flow using spectral analysis. *Meas Sci Technol* 8:1427–1440
- Gharib M (1987) Response of the cavity shear layer oscillations to external forcing. *AIAA J* 25:43–47
- Ghoniem A, Park S, Wachsman A, Annaswamy A, Wee D, Altay HM (2005) Mechanism of combustion dynamics in a backward-facing step stabilized premixed flame. *Proc Combust Inst* 30:1783–1790
- Ho C, Huerre P (1984) Perturbed free shear layers. *Ann Rev Fluid Mech* 16(1):365–422
- Johchi A, Naka Y, Shimura M, Tanahashi M, Miyauchi T (2015) Investigation on rapid consumption of fine scale unburned mixture islands in turbulent flame via 10 khz simultaneous CH-OH PLIF and SPIV. *Proc Combust Inst* 35(3):3663–3673
- Hsu K, Goss L, Trump D, Roquemore W (1998) Characteristics of a Trapped Vortex Combustor. *J Propuls Power* 14(1):57–65
- Johchi A, Naka Y, Shimura M, Tanahashi M, Miyauchi T (2015) Investigation on rapid consumption of fine scale unburned mixture islands in turbulent flame via 10 khz simultaneous CH-OH PLIF and SPIV. *Proc Combust Inst* 35(3):3663–3673
- Kaminski C, Hult J, Alden M (1999) High repetition rate planar laser-induced fluorescence of OH in a turbulent non-premixed flame. *Appl Phys B* 68:757–760
- Koenig K, Roshko A (1985) An experimental study of geometrical effects on the drag and flow field of two bluff bodies separated by a gap. *J Fluid Mech* 156:167–204
- Kumar PE, Mishra D (2011a) Numerical modeling of an axisymmetric trapped vortex combustor. *Int J Turbo Jet-Engines* 28:41–52
- Kumar PE, Mishra D (2011b) Numerical simulation of cavity flow structure in an axisymmetric trapped vortex combustor. *Aeros Sci Technol* 21(1):16–23
- Lieuwen T (2012) *Unsteady combustor physics*. Cambridge University Press, Cambridge
- Little B, Whipkey R (1979) Locked vortex afterbodies. *J Aircr* 16(5):296–302
- Merlin C (2012) *Simulation numérique de la combustion turbulente: Méthode de frontières immergées pour les écoulements compressibles, application à la combustion en aval d'une cavité*. Ph.D. thesis, INSA Rouen, France
- Najm H, Paul P, Mueller C, Wyckoff P (1998) On the adequacy of certain experimental observables as measurements of flame burning rate. *Combust Flame* 113(3):312–332
- Otsu N (1979) A threshold selection method from grey-level histograms. *IEEE Trans Syst Man Cybern* 9(1):62–66
- Charbonnier P, Blanc-feraud L, Aubert G, Barlaud M (1994) Two deterministic half-quadratic regularization algorithms for computed imaging. In: *Image Processing, 1994. Proceedings. ICIP-94., IEEE International Conference, vol 2, IEEE*, pp 168–172
- Peters N (2000) *Turbulent combustion*. Cambridge University Press, Cambridge
- Peterson B, Reuss D, Sick V (2014) On the ignition and flame development in a spray-guided direct-injection spark-ignition engine. *Combust Flame* 161(1):240–255
- Pitz R, Daily J (1983) Combustion in a turbulent mixing layer formed at a rearward-facing step. *AIAA J* 21:1565–1570
- Rockwell D, Knisely C (1979) The organized nature of flow impingement upon a corner. *J Fluid Mech* 93(03):413–432
- Roquemore W, Shouse D, Burns D, Johnson A, Cooper C, Duncan B, Hsu K, Katta V, Sturgess G, Vihinen I (2001) Trapped Vortex Combustor concept for gas turbine engines. In: *39th AIAA Aerospace Sciences Meeting and Exhibit*. Reno, NV, USA, pp 2001–0489
- Steinberg A, Boxx I, Arndt C, Franck J, Meier W (2011) Experimental study of flame-hole reignition mechanisms in a turbulent non-premixed jet flame using sustained multi-kHz PIV and crossed-plane OH PLIF. *Proc Combust Inst* 33(1):1663–1672

- Stohr M, Boxx I, Carter C, Meier W (2011) Dynamics of lean blow-out of a swirl-stabilized flame in a gas turbine model combustor. *Proc Combust Inst* 33(2):2953–2960
- Straub D, Casleton K, Lewis R, Sidwell T, Maloney D, Richards G (2005) Assessment of Rich-burn, Quick-mix, Lean-burn Trapped Vortex Combustor for stationary gas turbines. *J Eng Gas Turbines Power* 127(1):36–41
- Trunk P, Boxx I, Heeger C, Meier W, Bohm B, Dreizler A (2013) Premixed flame propagation in turbulent flow by means of stereoscopic PIV and dual-plane OH-PLIF at sustained khz repetition rates. *Proc Combust Inst* 34(2): 3565–3572
- Sun M, Cui X, Wang H, Bychkov V (2015) Flame flashback in a supersonic combustor fueled by ethylene with cavity flameholder. *J Jet Propuls* 31(3):976–981
- Taupin B, Cabot G, Martins G, Vauchelles D, Boukhalfa A (2007) Experimental study of stability, structure and CH\* chemiluminescence in a pressurized lean premixed methane turbulent flame. *Combust Sci Technol* 179:117–136
- Trunk P, Boxx I, Heeger C, Meier W, Bohm B, Dreizler A (2013) Premixed flame propagation in turbulent flow by means of stereoscopic PIV and dual-plane OH-PLIF at sustained khz repetition rates. *Proc Combust Inst* 34(2):3565–3572
- Upanietks A, Driscoll J, Ceccio S (2002) Cinema particle imaging velocimetry time history of the propagation velocity of the base of a lifted turbulent jet flame. *Proc Combust Inst* 29:1897–1903
- Weickert J (1997) A review of nonlinear diffusion filtering. In: *Scale-space theory in computer vision*. Springer, Berlin, Heidelberg, pp 1–28
- Welch P (1967) The use of Fast Fourier Transform for the estimation of power spectra: a method based on time averaging over short, modified periodograms. *IEEE Trans Audio Electroacoust* 15:70–73
- Wulff A, Hourmouziadis J (1997) Technology review of aeroengine pollutant emissions. *Aeros Sci Technol* 8:557–572
- Yuan Y, Zhang T, Yao W, Fan X (2015) Study on flame stabilization in a dual-mode combustor using optical measurements. *J Propuls Power* 31(6):1524–1531